

3D Flapping Wing Simulation with High Order Spectral Difference Method on Deformable Mesh

K. Ou*, P. Castonguay† and A. Jameson‡

Aeronautics and Astronautics Department, Stanford University, Stanford, CA 94305

In this paper we carry out computational studies of three-dimensional flow over flapping wings. The problems we have investigated include, firstly, three-dimensional simulation of flow over an extruded SD7003 airfoil in plunging motion at transitional Reynolds number and, secondly, flow over a pair of flapping rectangle wings with constant NACA0012 cross-sectional airfoil profile at low Reynolds number. The three-dimensional flapping wing simulations are performed using high-order spectral difference method at low Mach number. The high-order method allows a very coarse starting mesh to be used. By using high order solution, fine flow features in the vortex-dominated flow field are effectively captured. For the plunging SD7003 airfoil, we examine the laminar to turbulence flow transitional behavior at Re 40,000. For the NACA0012 rectangular wing, we analyze and compare the flow fields and aerodynamic efficiencies of several flapping wing motions at Re 2000. The flapping motions considered include wing plunging, twisting and pitching. Some of the flapping wing motions are accommodated through dynamic mesh deformation.

I. Introduction

Flapping wing differs from fixed wing in the regard that it performs an integrated function of supporting weight through lift and providing propulsion through thrust. This is commonly found in natural flyers such as birds and insects. Despite flapping flight being widely adapted in nature, its understanding still poses great challenges for biologists and aerodynamicists. Flapping wing aerodynamic has proved to be more challenging than the traditional fixed wing aerodynamic. Not only is the fluid mechanics of flapping flight more complicated, experimental study of flapping wing vehicles is also more difficult to perform in wind tunnel than conventional airplanes. This leads to a shortage of experimental flapping flight test data.

The fluid mechanics of flapping flight is not well understood due to the complex unsteady fluid physics at low Reynolds number. The flow tends to be heavily vortex dominated and sometimes exhibits transitional behavior. It is further complicated by the intricate interaction between flexible wing structure and the surrounding fluid. A lot of work has been done, by biologists and engineers alike, to extend the understanding of animal flight. Study on trained animals in wind tunnel can be advantageous both in simulating the actual flight and in avoiding developing complicated physical flapping wing model. However, there are great difficulties working with animals and extracting useful information becomes challenging when there are many limitations to what can be measured on real birds.

The motivation of the current study originates from the increasing interest to advance the design knowledge of Micro Air Vehicles based on flapping wings. Micro Air Vehicles have been the subject of extensive research and development over the last several years. Research have been driven in part by the civil and military desires to build small vehicles to operate in hostile or urban environments. Some successful MAVs have been built. A few examples include BlackWidow and MicroBat. The benefits of a flapping wing MAV include its quiet operation, its ability to carry out short take off and landing, and its capability for impressive maneuver and hovering. The challenge lies in the lack of efficient analytical tools, and the shortage of experimental wind tunnel and flight test data. It is also very difficult to model the biological wing due to its complex design and flexible nature. Equally challenging is the ability to simulate the motion of a biological

*PhD Candidate, Aeronautics and Astronautics Department, Stanford University, AIAA Student Member.

†PhD Candidate, Aeronautics and Astronautics Department, Stanford University, AIAA Student Member.

‡Thomas V Jones Professor, Aeronautics and Astronautics Department, Stanford University, AIAA Fellow.

flapping wing, which undergoes constant changes to optimize the flight. Computational fluid dynamics and optimization tools provide a path to analyze flapping aerodynamics and subsequently design highly efficient flapping wing vehicle. While computational cost for full 3D simulation is still huge and remains a challenge to be overcome, rapid growth of computational processing power, as well as the emergence of Graphic Processing Units (GPUs), when combined with more efficient algorithms, make it feasible to conduct full 3D Direct Numerical Simulation (DNS) of such a problem in the Reynolds number regime relevant to flapping flight. Work towards this goal has been led by Peraire, Willis, Persson, Drela et al^{1,2} to explore effective flapping wing vehicle using a multifidelity framework. The recent study by Persson, Willis, and Peraire⁸ compared a low fidelity but computationally efficient panel code with a high fidelity but expensive Navier-Stokes solver for simulating a full 3D flapping wings with prescribed flapping and twisting motion, demonstrating the capability of the state of the art CFD solver. To align with the research in this direction, in this paper we consider the application of the high order spectral difference solver for the direct simulation of 3D flapping wing. In particular, we are interested in examining the transitional flow behavior and the aerodynamic characteristics of various flapping motions.

This paper is organized in the following order. We start by a short description of the computational mesh used. The spectral difference method for the 3D Navier-Stokes equations is presented next. This is followed by a brief discussion of mesh deformation method and the extension of the spectral difference formulation to deforming mesh. In the validation section, we present the three-dimensional simulation of flow over a stationary SD7003 airfoil. The accuracy of the present 3D solver and the ability to resolve some transitional flow phenomenon are discussed. In the results section, we first present the simulation results of three-dimensional flow over a plunging SD7003 airfoil at Re 40000. Flow over a flapping rectangular wing with constant NACA0012 airfoil cross-section is discussed last.

II. Computational Setup

II.A. SD7003 Airfoil Geometry and Mesh

For the purpose of numerical validation, we performed 3D computations for the steady flow over an extruded SD7003 airfoil. The SD7003 airfoil mesh has a C topology. The mesh is extended in the spanwise direction by $0.2c$, where c is the chord length, to accommodate spanwise flow. The same mesh is used for the subsequent 3D unsteady simulation of flow over the plunging SD7003 airfoil. Figure 1 shows the mesh near the airfoil surface in (a) and the mesh in the flow domain in (b). Figure 1 (a) also gives an example of the way the mesh is partitioned for parallel computation. This will be discussed further.

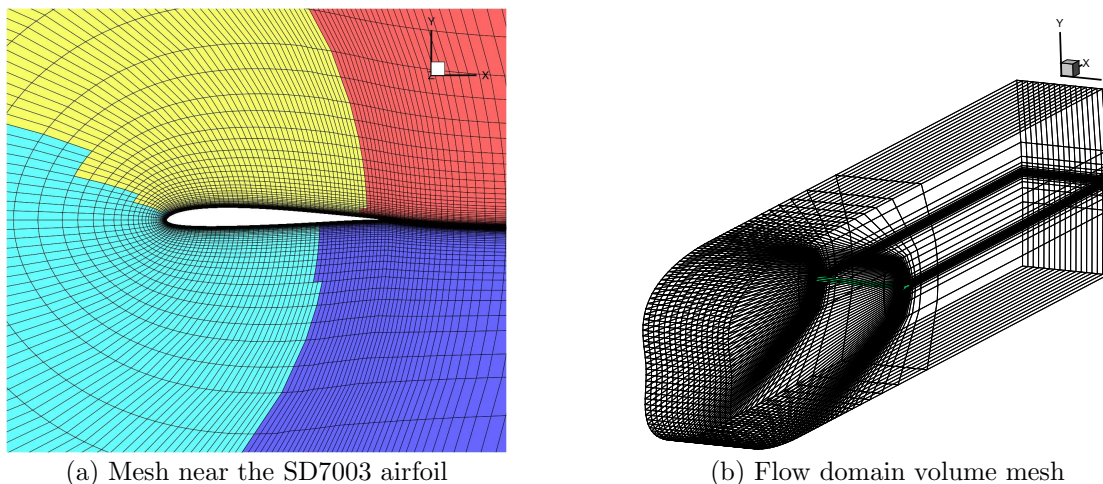


Figure 1. Computation mesh of SD7003 airfoil

II.B. Naca0012 Wing Geometry and Mesh

The rectangular wing used in this study has a constant cross-sectional NACA0012 airfoil profile. The chord has a length of 1. The wing span from tip to root is 4. The flow inlet is 15 chord away, the outlet is 10

chord away, and the spanwise freestream boundary is 7 chord away from the tip of the wing. Figure 2 shows the starting coarse mesh used for the subsequent high order simulations. The starting mesh has a total of 37,704 mesh cells.

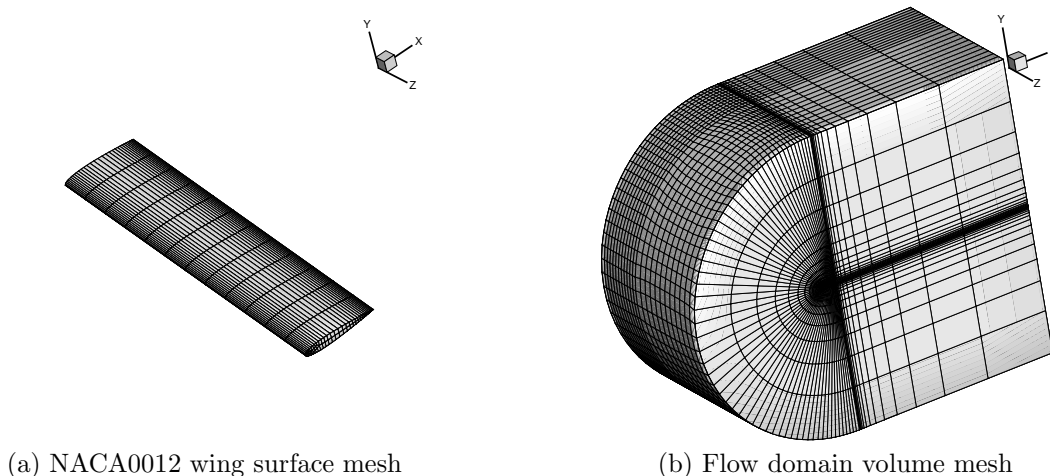


Figure 2. Computation mesh of the NACA0012 wing

Note in both cases, high order curved boundary representation are implemented.

II.C. Plunging Motion of the SD7003 Airfoil

For the plunging SD7003 airfoil, the plunging motion is described by

$$h = h_0 \cos(2\pi ft)$$

where $h_0=0.05$ and $f=\frac{kU_\infty}{\pi}$, with $k=3.93$ and $U_\infty = 0.1$.

II.D. Flapping Motions of the NACA0012 Wing

For the flapping wing simulations of the NACA0012 wing, three flapping wing motions are considered. In the first case, the pair of wings is plunging as a rigid body according to the following function

$$h = h_0 \sin(2\pi ft)$$

where $h_0=0.75$ and $f=\frac{StrU_\infty}{h_0}$, with $Str=0.2$ and $U_\infty = 0.1$. In the second case, the pair of wings is plunging as a rigid body while at the same time pitching along the z -axis at $1/3$ of the chord from the leading edge. The plunging motion is the same as the previous case. The z -axis pitching angle is described by

$$\theta_z = \theta_{z0} \sin(2\pi ft + \Phi)$$

where $\theta_{z0}=15^\circ$ and $f=\frac{StrU_\infty}{h_0}$, with $Str=0.2$ and $U_\infty = 0.1$ as before. $\Phi=75^\circ$ describes the phase lead of the z -axis pitching over the plunging motion. In the third case, the pair of wings is purely pitching along the x -axis in the center line. The x -axis pitching angle is described by

$$\theta_x = \theta_{x0} \sin(2\pi ft)$$

where $\theta_{x0}=10.8^\circ$ and $f=\frac{StrU_\infty}{h_0}$, with $Str=0.2$ and $U_\infty = 0.1$. The resulting pitching motion also has a maximum tip amplitude of 0.75 , as in the previous two cases.

II.E. 3D Spatial Discretization with Spectral Difference Method

In the present work, the Navier-Stokes equations are solved using the high-order Spectral Difference method for spatial discretization. The formulation of the equations on hexahedral grids is similar to the formulation of Liu et al.,³ which will be summarized below for completeness.

Consider the unsteady compressible Navier-Stokes equations in conservative form written as:

$$\frac{\partial Q}{\partial t} + \frac{\partial F}{\partial x} + \frac{\partial G}{\partial y} + \frac{\partial H}{\partial z} = 0 \quad (1)$$

where $F = F_I - F_V$, $G = G_I - G_V$ and $H = H_I - H_V$. To achieve an efficient implementation, all element in the physical domain (x, y, z) are transformed into a standard cubic element, $0 \leq \xi \leq 1, 0 \leq \eta \leq 1, 0 \leq \zeta \leq 1$. The transformation can be written as

$$\begin{pmatrix} x \\ y \\ z \end{pmatrix} = \sum_{i=1}^K M_i(\xi, \eta, \zeta) \begin{pmatrix} x_i \\ y_i \\ z_i \end{pmatrix} \quad (2)$$

where K is the number of points used to define the physical elements, (x_i, y_i, z_i) are the Cartesian coordinates at those points, and $M_i(\xi, \eta, \zeta)$ are the shape functions. The metrics and Jacobian of the transformation can be computed for the standard element. The governing equations in the physical domain are then transferred into the computational domain, and the transformed equations take the following form:

$$\frac{\partial \tilde{Q}}{\partial t} + \frac{\partial \tilde{F}}{\partial \xi} + \frac{\partial \tilde{G}}{\partial \eta} + \frac{\partial \tilde{H}}{\partial \zeta} = 0 \quad (3)$$

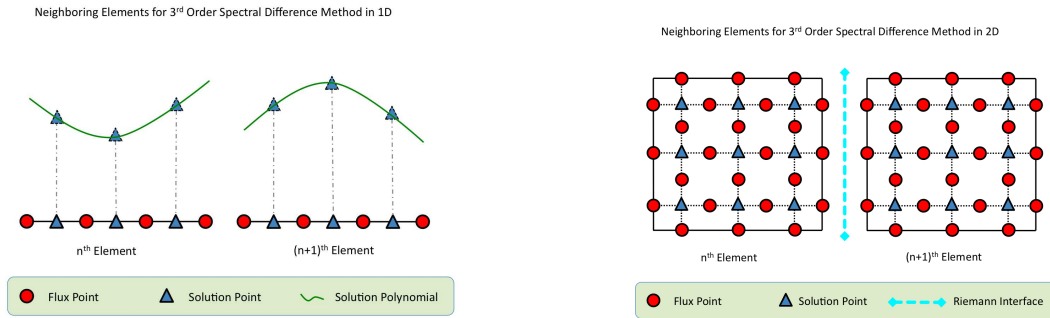
where $\tilde{Q} = |J|Q$ and

$$\begin{pmatrix} \tilde{F} \\ \tilde{G} \\ \tilde{H} \end{pmatrix} = |J| \begin{pmatrix} \xi_x & \xi_y & \xi_z \\ \eta_x & \eta_y & \eta_z \\ \zeta_x & \zeta_y & \zeta_z \end{pmatrix} \begin{pmatrix} F \\ G \\ H \end{pmatrix} \quad (4)$$

The Jacobian matrix J is given by

$$J = \frac{\partial(x, y, z)}{\partial(\xi, \eta, \zeta)} = \begin{pmatrix} x_\xi & x_\eta & x_\zeta \\ y_\xi & y_\eta & y_\zeta \\ z_\xi & z_\eta & z_\zeta \end{pmatrix} \quad (5)$$

In the standard element, two sets of points are defined, namely the solution points and the flux points, as illustrated in Figure 3 for a 2D element. In order to construct a degree $(N - 1)$ polynomial in each coordinate



(a) 3rd order SD in 1D element

(b) 3rd order SD in 2D element

Figure 3. Position of solution (triangles) and flux (circles) points on the standard 1D (left) and 2D (right) element for 3rd order SD

direction, solution at N points are required. The solution points in 1D are chosen to be the Gauss points defined by:

$$X_s = \frac{1}{2} \left[1 - \cos \left(\frac{2s-1}{2N} \pi \right) \right], s = 1, 2, \dots, N. \quad (6)$$

The flux points were selected to be the Legendre-Gauss quadrature points plus the two end points 0 and 1, as suggested by Huynh.⁴ Choosing $P_{-1}(\xi) = 0$ and $P_0(\xi) = 1$, the higher-degree Legendre polynomials are

$$P_n(\xi) = \frac{2n-1}{n}(2\xi-1)P_{n-1}(\xi) - \frac{n-1}{n}P_{n-2}(\xi) \quad (7)$$

The locations of these Legendre-Gauss quadrature points are the roots of equations $P_n(\xi) = 0$. Jameson⁵ proved that this particular choice of flux point leads to energy stable spectral difference scheme. Using the solutions at N solution points, a degree $(N-1)$ polynomial can be built using the following Lagrange basis defined as:

$$h_i(X) = \prod_{s=1, s \neq i}^N \left(\frac{X - X_s}{X_i - X_s} \right) \quad (8)$$

Similarly, using the fluxes at $(N+1)$ flux points, a degree N polynomial can be built for the flux using a similar Lagrange basis as:

$$l_{i+1/2}(X) = \prod_{s=0, s \neq i}^N \left(\frac{X - X_{s+1/2}}{X_{i+1/2} - X_{s+1/2}} \right) \quad (9)$$

The reconstructed solution for the conserved variables in the standard element is the tensor product of the three one-dimensional polynomials,

$$Q(\xi, \eta, \zeta) = \sum_{k=1}^N \sum_{j=1}^N \sum_{i=1}^N \frac{\tilde{Q}_{i,j}}{|J_{i,j}|} h_i(\xi) h_j(\eta) h_k(\zeta) \quad (10)$$

Similarly, the reconstructed flux polynomials take the following form:

$$\begin{aligned} \tilde{F}(\xi, \eta, \zeta) &= \sum_{k=1}^N \sum_{j=1}^N \sum_{i=0}^N \tilde{F}_{i+1/2,j,k} \cdot l_{i+1/2}(\xi) \cdot h_j(\eta) \cdot h_k(\zeta) \\ \tilde{G}(\xi, \eta, \zeta) &= \sum_{k=1}^N \sum_{j=0}^N \sum_{i=1}^N \tilde{G}_{i,j+1/2,k} \cdot h_i(\xi) \cdot l_{j+1/2}(\eta) \cdot h_k(\zeta) \\ \tilde{H}(\xi, \eta, \zeta) &= \sum_{k=0}^N \sum_{j=1}^N \sum_{i=1}^N \tilde{H}_{i,j,k+1/2} \cdot h_i(\xi) \cdot h_j(\eta) \cdot l_{k+1/2}(\zeta) \end{aligned} \quad (11)$$

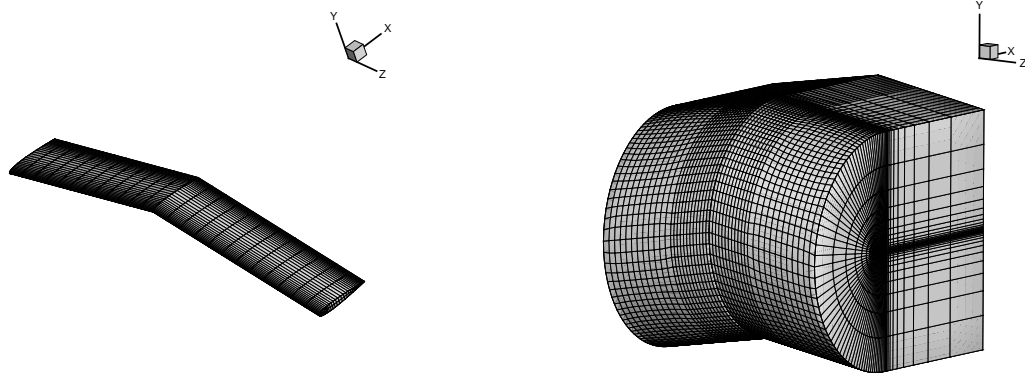
The reconstructed fluxes are only element-wise continuous, but discontinuous across cell interfaces. For the inviscid flux, a Riemann solver is employed to compute a common flux at interfaces to ensure conservation and stability. In our case, we have used both the Rusanov solver⁶ and the Roe⁷ solver to compute the interface inviscid fluxes. The viscous flux is a function of both the conserved variables and their gradients. Therefore, the solution gradients have to be calculated at the flux points. In our solver, the average approach described in reference³ is used to compute the viscous fluxes.

III. Mesh Deformation

While wing plunging motion and wing pitching motion of the rigid wing along the z-axis can be achieved by rigid translation and rotation of the entire flow domain volume mesh, the pitching motion along the wing root center line needs to be accommodated through some mesh deformations. A simple algebraic way to achieve this is used by Persson, Willis, and Peraire.⁸ The pitching motion is achieved through a combination of mesh shearing and dilation. This also helps to preserve the volume of the flapping wing. An example of the resulting mesh using this method is shown in figure 4. The method is outlined next.

Define the deformed physical mesh by $(x, y, z)^p$, the original undisplaced mesh by (x^r, y^r, z^r) , the rotational angle by θ , and the center of mesh rotation by (x_0^r, y_0^r, z_0^r) , the transformation from the stationary reference mesh to the deformed mesh can now be represented as

$$\begin{bmatrix} x^p \\ y^p \\ z^p \end{bmatrix} = \begin{bmatrix} x^r \\ y^r \\ z^r \end{bmatrix} + \begin{bmatrix} 1 & 1 & 0 \\ 0 & \sec\theta_x & \tan\theta_x \\ 0 & 0 & \cos\theta_x \end{bmatrix} \begin{bmatrix} x^r - x_0^r \\ y^r - y_0^r \\ z^r - z_0^r \end{bmatrix} \quad (12)$$



(a) Pitching wing surface mesh

(b) Pitching wing flow domain volume mesh

Figure 4. Computation mesh of a pitching NACA0012 wing

IV. SD Extension to Moving Deforming Mesh Problem

In order to formulate SD on a dynamic deforming mesh, we first consider the fact that a moving mesh at any new time instance leads to a new coordinate system. Hence one way to formulate the conservation laws with SD on deformable mesh is to implement unsteady coordinate transformation. The time-dependent transformation allows the boundary disturbance to propagate through the flow domain without deteriorating the accuracy of the spatial discretization method. The details of coordinate transformation and the corresponding transformation of conservation laws are outlined in the subsequent sections.

IV.A. Time-dependent Coordinate Transformation

When the two coordinate systems are moving relative to one another, the unsteady transformation \mathbf{T}_u is now time dependent. Let's consider the unsteady coordinate transformation between the physical space in (x, y, z) and the reference space in (X, Y, Z) .

$$(X, Y, Z) = \mathbf{T}_u(x, y, z, t) \quad (13)$$

and we have:

$$X = X(x, y, z, t), \quad Y = Y(x, y, z, t), \quad Z = Z(x, y, z, t)$$

Again using the chain rule to arrive at the unsteady transformation gradient as:

$$\mathbf{G}_{\mathbf{T}_u} = \begin{bmatrix} \frac{\partial x}{\partial X} & \frac{\partial y}{\partial X} & \frac{\partial z}{\partial X} \\ \frac{\partial x}{\partial Y} & \frac{\partial y}{\partial Y} & \frac{\partial z}{\partial Y} \\ \frac{\partial x}{\partial Z} & \frac{\partial y}{\partial Z} & \frac{\partial z}{\partial Z} \end{bmatrix} \quad (14)$$

The Jacobian of the unsteady transformation gradient is equal to:

$$J_{T_u} = \det|G_{T_u}| \quad (15)$$

IV.B. Navier-Stokes Equations in Transformed Reference Space

In the unsteady case, using the chain rule for differentiation, and define the following new identities

$$\mathbf{U}^{\mathbf{r}} = J_{T_u} \mathbf{U}^{\mathbf{p}}$$

$$\mathbf{F}^{\mathbf{r}} = J_{T_u} \left(\mathbf{F}^{\mathbf{p}} \frac{\partial X}{\partial x} + \mathbf{G}^{\mathbf{p}} \frac{\partial X}{\partial y} + \mathbf{H}^{\mathbf{p}} \frac{\partial X}{\partial z} + \mathbf{U}^{\mathbf{p}} \frac{\partial X}{\partial t} \right) \quad (16)$$

$$\mathbf{G}^r = J_{Tu}(\mathbf{F}^p \frac{\partial Y}{\partial x} + \mathbf{G}^p \frac{\partial Y}{\partial y} + \mathbf{H}^p \frac{\partial Y}{\partial z} + \mathbf{U}^p \frac{\partial Y}{\partial t})$$

$$\mathbf{H}^r = J_{Tu}(\mathbf{F}^p \frac{\partial Z}{\partial x} + \mathbf{G}^p \frac{\partial Z}{\partial y} + \mathbf{H}^p \frac{\partial Z}{\partial z} + \mathbf{U}^p \frac{\partial Z}{\partial t})$$

where superscript p denotes variables in the physical domain, while superscript r denotes variables in the reference domain. The governing equation in the new reference coordinate space in the unsteady case still assumes the same conservation law form:

$$\frac{\partial \mathbf{U}^r}{\partial t} + \frac{\partial \mathbf{F}^r}{\partial X} + \frac{\partial \mathbf{G}^r}{\partial Y} + \frac{\partial \mathbf{H}^r}{\partial Z} = 0 \quad (17)$$

Note that the entire computation is carried out based on the reference domain. When physical space solution is needed, the computed reference space solution can be readily mapped using the mapping Jacobians.

V. Domain Decomposition and Parallelization

The spectral difference method is a highly efficient high-order accurate method that is well suited for large-scale time-dependent computations in which high accuracy is required. The discontinuous nature of the spectral difference scheme and the fact that the current implementation of the 3D spectral difference method uses an explicit time advancement scheme makes our current 3D code well suited for parallel computer platforms. In the following paragraph, the parallel implementation of the 3D spectral difference code will be discussed.

First, the domain is partitioned using the graph partitioning code METIS. An example of the partitioning obtained for the mesh used is shown in Figure 5.

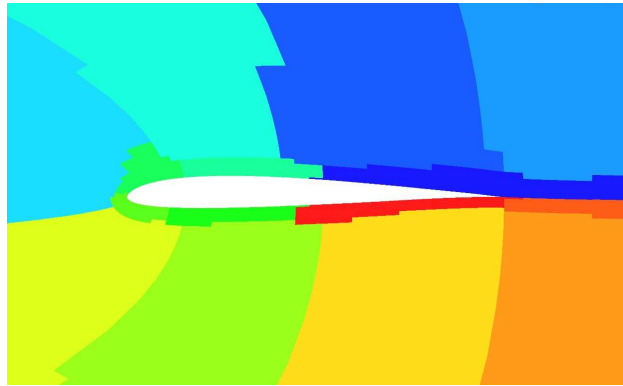


Figure 5. Partitions obtained from graph partitioning software METIS

Once the domain is decomposed, each processor updates the solution at the interior points of the cells in its domain following the same procedure as in the serial code. For element interfaces that are adjacent to a partition boundary, non-blocking sends and receives are used to exchange the right and left state vector Q^L and Q^R , along with the gradient of the state vectors ∇Q^R and ∇Q^L , so that the procedure to compute the flux values at the interface can be applied. The MPI-based parallelization of the code is thus highly efficient due to the non-blocking strategy used.

VI. Time Integration Method

All computations in this paper are advanced in time using a fourth-order strong-stability-preserving five-stage Runge-Kutta scheme. For unsteady boundary moving problems, the deforming mesh is changing in time. The transformation metrics for the rigidly displaced and deforming meshes need to be updated at every stage of the Runge-Kutta to pass the unsteady information from the moving physical domain to

the stationary reference domain, where computation is carried out. This also helps to preserve the formal temporal accuracy of the Runge-Kutta scheme. The transformation metrics, velocities, and Jacobian are calculated using the methods outlined in the previous section on unsteady transformations.

VII. Numerical Validation

Flow over Stationary SD7003 Wing

Flow over stationary SD7003 airfoil at an angle of attack of 4° at Reynolds number of 10000 and 60000 was first calculated using the SD3D method by Castonguay, Liang and Jameson.⁹ A 4th order accurate solution was obtained. In order to reduce the computational cost associated with initial transients from an uniform initial solution, two-dimensional solutions were used for the initial condition on the three-dimensional mesh. All mean values were calculated by averaging the spanwise averaged time accurate solution over a non-dimensional time interval of around 8. A non-dimensional time step of $2 \cdot 10^{-5}$ was used and solution was recorded at every 1000 steps for the computation of the mean values.

VII.A. Reynolds Number=10000

At this Reynolds number, the flow is essentially two-dimensional with close-to-periodic vortex shedding. Figure 6 a) and b) shows the history of lift and drag coefficients respectively, after the initial transients from a freestream initial solution have vanished. Figure 6 c) shows the mean surface coefficient of pressure obtained from the SD3D code. The average drag and lift coefficient, as well as the Cp plot obtained with the Spectral Difference method matches the results obtained by Urange et al.¹² using a Discontinuous Galerkin approach. As presented in Figure 7 a), which shows average Mach contours, the boundary layer separates at 0.342 chords from the leading edge and does not reattach. Furthermore, the flow remains laminar over the airfoil as seen by looking at contours of the Reynolds shear stress in Figure 7 b). Transition is said to occur when the Reynolds shear stress reaches a value of 0.1% and exhibits a clear visible rise. The flow becomes turbulent only at the trailing edge, where the boundary layers on the upper and lower surfaces meet. The Q-criterion also provides a mean of visualizing vortex cores and identify turbulent structures. It can be calculated from:

$$Q = \frac{1}{2}(\Omega_{ij}\Omega_{ij} - S_{ij}S_{ij}) \quad (18)$$

where Ω_{ij} and S_{ij} are the anti-symmetric and symmetric of the velocity gradient tensor.

$$\Omega_{ij} = \frac{1}{2} \left(\frac{\partial u_i}{\partial x_j} - \frac{\partial u_j}{\partial x_i} \right) \text{ and } S_{ij} = \frac{1}{2} \left(\frac{\partial u_i}{\partial x_j} + \frac{\partial u_j}{\partial x_i} \right) \quad (19)$$

Figure 7 c) shows instantaneous iso-surfaces of Q-criterion and shows no spanwise variation over the surface of the airfoil.

VII.B. Reynolds Number=60000

At a Reynolds number of 60000, transition takes place across a laminar separation bubble (LSB) over the airfoil. Again, computations were performed on a mesh with 1.7 million degrees of freedom. Figure 8 a) and b) shows the time history of the lift and drag coefficients. The average lift and drag coefficients were 0.610 and 0.229, respectively. The average pressure coefficient on the airfoil at this Reynolds number is presented in Figure 8 c). The pressure gradient in the transition region is steeper than the one obtained by Urange et al.¹² and matches very well the one obtained by Galbraith and Visbal¹³ who used a 6th order spatial discretization on an overset mesh. A comparison of separation, transition and reattachment locations is given in Table 1. These values were obtained by looking at the streamlines of the mean velocity profile shown in figure 9 a) and contours of the Reynolds shear stress in figure 9 b). Results obtained with the Spectral Difference method by means of a ILES are in excellent agreement with the experimental results obtained by Radiespel et al.¹¹ and the computational results of Visbal et al.¹³ Thus, even though the grid resolution is clearly too coarse to capture all scales of motion, the proposed method appears to accurately predict the laminar separation and subsequent transition to turbulent flow. Finally, figures 9 c) shows instantaneous iso-surfaces of the Q-criterion and vorticity. Three-dimensional structures associated with transition to turbulent flow can easily be identified in these figures.

Data Set	Freestream Turbulence	Separation x_{sep}	Transition x_{tr}/c	Reattachment x_r/c
TU-BS ¹¹	0.08%	0.30	0.53	0.64
HFWT ¹⁰	0.1%	0.18	0.47	0.58
Visbal (ILES) ¹³	0	0.23	0.55	0.65
Uranga (ILES) ¹²	0	0.23	0.51	0.60
Present ILES	0	0.23	0.53	0.64

Table 1. Measured and Computed properties of flow over SD7003 at $Re=60000$, $\alpha = 4^\circ$

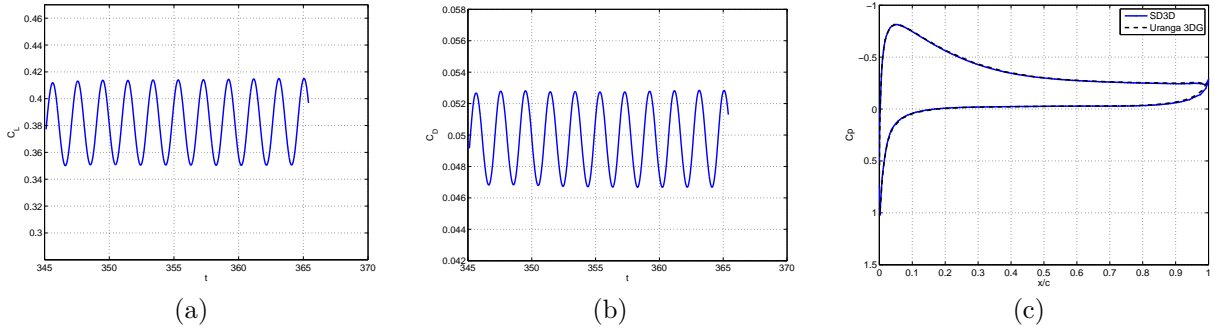


Figure 6. Time history of (a) lift coefficient and (b) drag coefficient for SD7003 airfoil (c) Average pressure coefficient

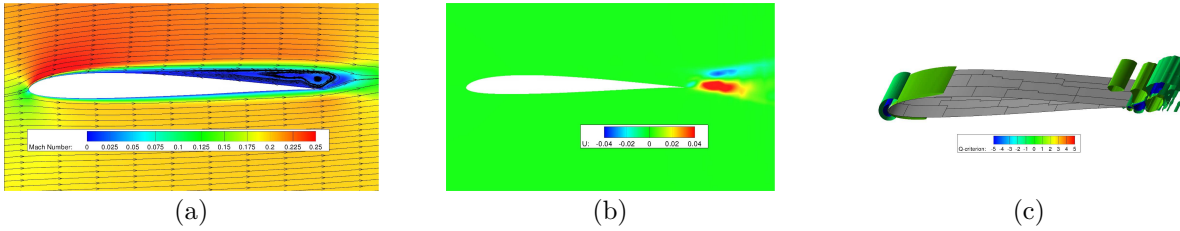


Figure 7. (a) Average Mach contours and streamlines (b) Reynolds shear stress ($\langle u'v' \rangle / U_\infty^2$) (c) Instantaneous iso-surfaces of Q-criterion at $Re=10000$

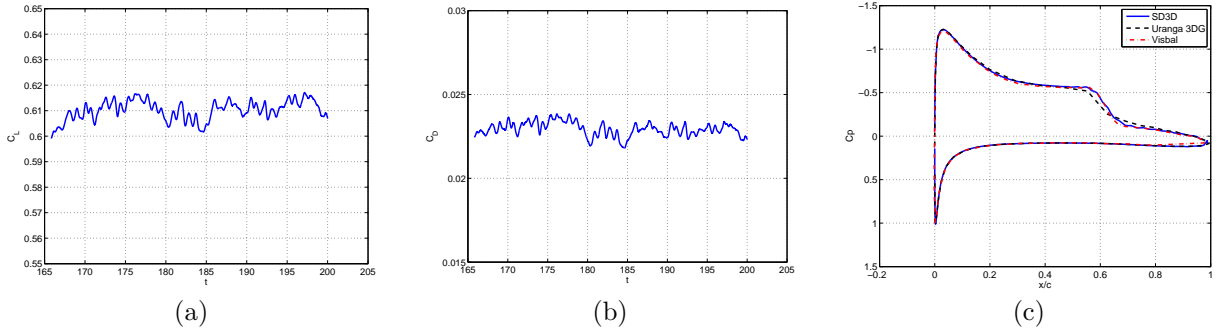


Figure 8. Time history of (a) lift coefficient and (b) drag coefficient for SD7003 airfoil (c) Average pressure coefficient

VIII. Numerical Results

VIII.A. Plunging SD7003 Airfoil

To investigate the ability of the current method to solve 3D unsteady flow and predict transitional phenomena, we consider in this study a flow past a plunging SD7003 wing at Reynolds number of 40,000. With experimental results available to compare with, this test case has been carefully examined by the referenced study.¹⁴ We show here that similar results can be obtained with our present 3D solver to account for both

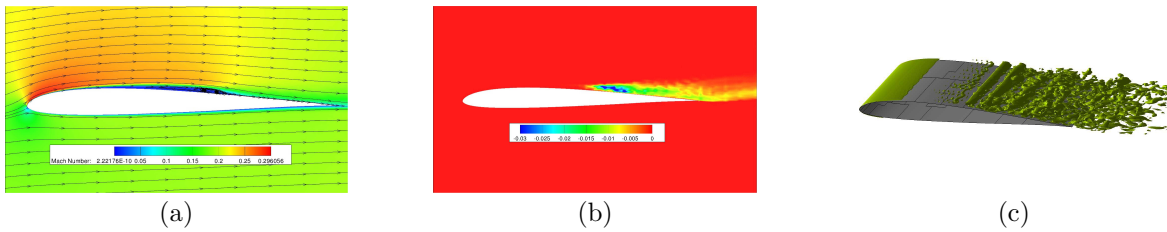


Figure 9. (a) Average Mach contours and streamlines (b) Reynolds shear stress ($\langle u'v' \rangle / U_\infty^2$) (c) Instantaneous iso-surfaces of Q-criterion at $Re=60000$

the plunging flow and the transitional behavior. The computational grid used here is the same as the one used previously for the steady example. The parameters that define the flow conditions are: $Mach=0.1$; $Re=40,000$; $k=3.93$; $\alpha_0=4deg$; $h_0/c=0.05$. We perform this simulation using a 4th order SD solution, with a total of 1.7 million degree of freedom. The aerodynamic lift and drag are plotted in Figure (11), together with the corresponding results from the referenced study. Very good agreements are obtained. In terms of

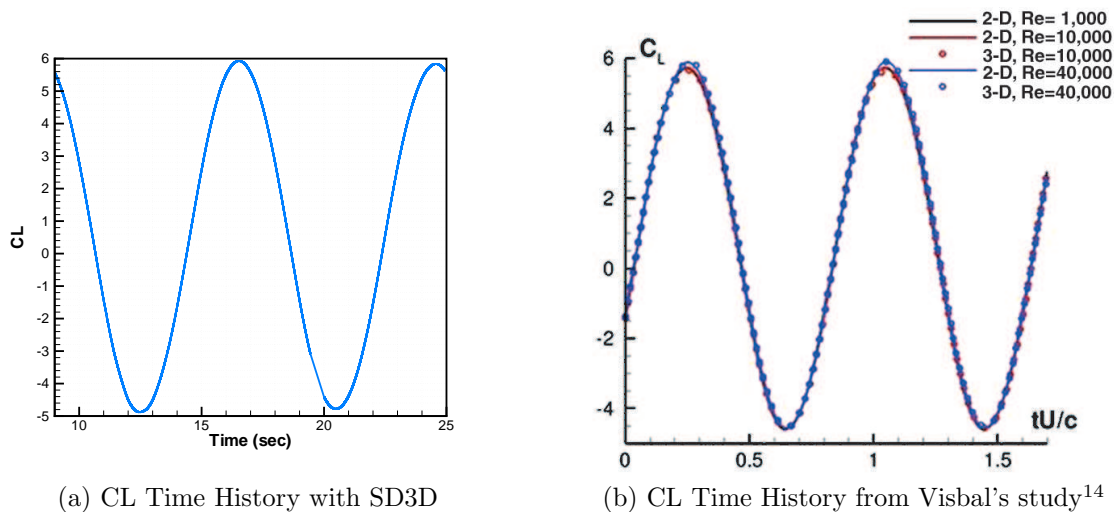


Figure 10. Aerodynamic Lift Time History for a Transitional Flow over a Plunging SD7003 Airfoil at $Re=40,000$

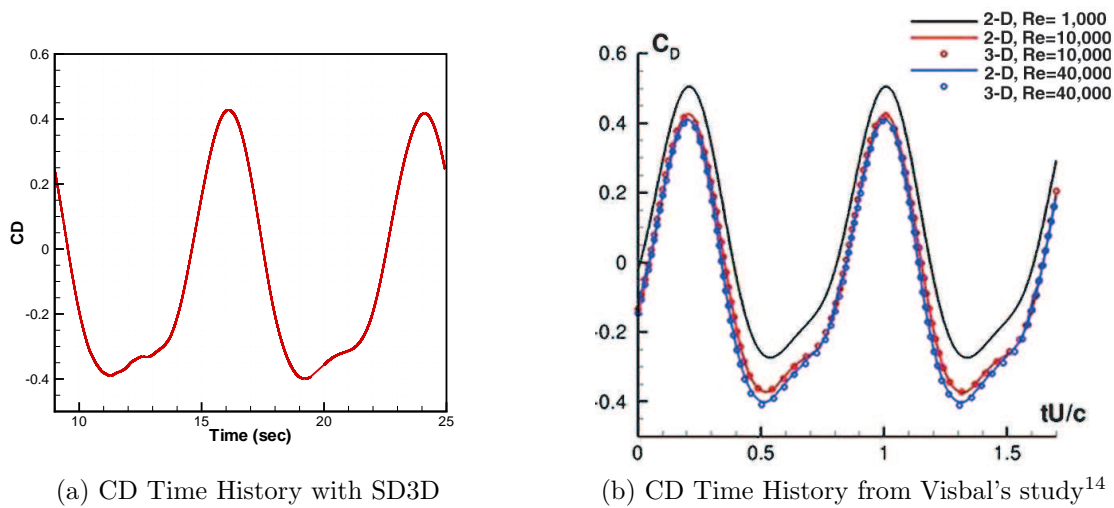


Figure 11. Aerodynamic Drag Time History for a Transitional Flow over a Plunging SD7003 Airfoil at $Re=40,000$

resolving the transitional flow from laminar to turbulent, the SD3D solver also produces results that exhibit the transitional behavior depicted by experiments as well as Visbal's computational study. The streamwise

flow velocity contours at different phases of a plunging cycle are plotted and compared with the referenced results in Figure (12).

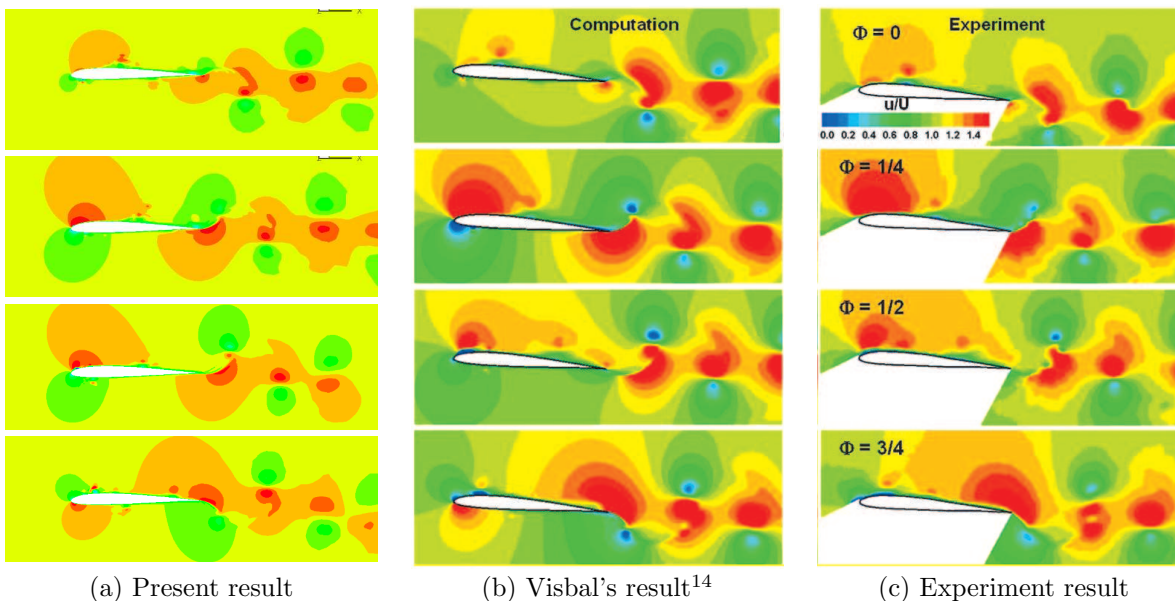


Figure 12. Streamwise Velocity Contour of a Transitional Flow over a Plunging SD7003 Airfoil at $Re=40,000$

To illustrate the occurrence of flow transition, the spanwise vorticity contours during the transitional process are shown in Figure (13). From the obtained results, we observe that the transitional process starts

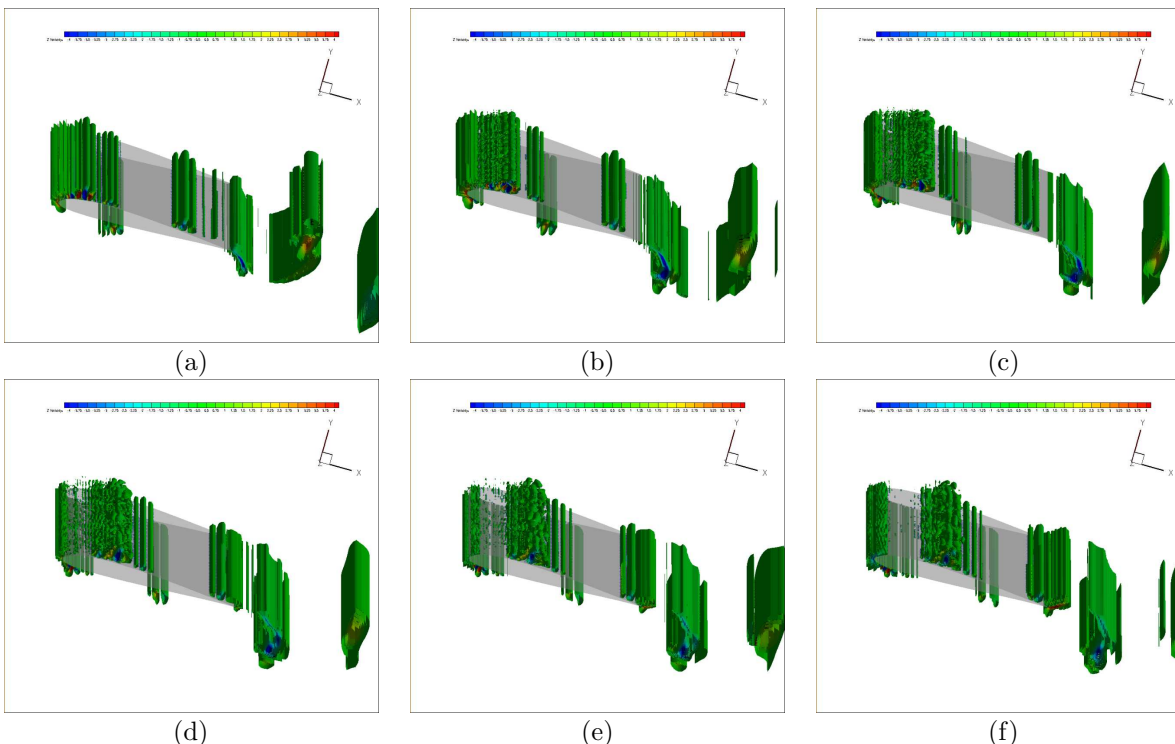


Figure 13. Spanwise Vorticity Contour of a Transitional Flow over a Plunging SD7003 Airfoil at $Re=40,000$. Plots (a)-(f) illustrate the process of flow transiting from laminar to turbulent.

with the formation of a large laminar flow bubble at the airfoil leading edge. This occurs at the bottom of the downstroke, as the airfoil reverses its direction and creates vortical flow near its surface. When the vortical bubble first forms at the leading edge, it begins to convect downstream. At the same time, the

airfoil is moving upwards, interacting with the laminar bubble. The resistance of the laminar bubble to the disturbance clearly depends on the flow properties, as defined by Reynolds number. In this particular case, the upward moving airfoil effectively disperses the coherent laminar bubble into many smaller turbulent structures, leading to flow transition.

VIII.B. Flapping Naca0012 Wing

The simulations for flow over the flapping Naca0012 wing have been performed with 5th order SD method. With 37,704 cells in the starting mesh, this corresponds to 4,713,000 degrees of freedom. Figure 14 plots three cut-planes of the computational mesh showing all the degrees of freedom.

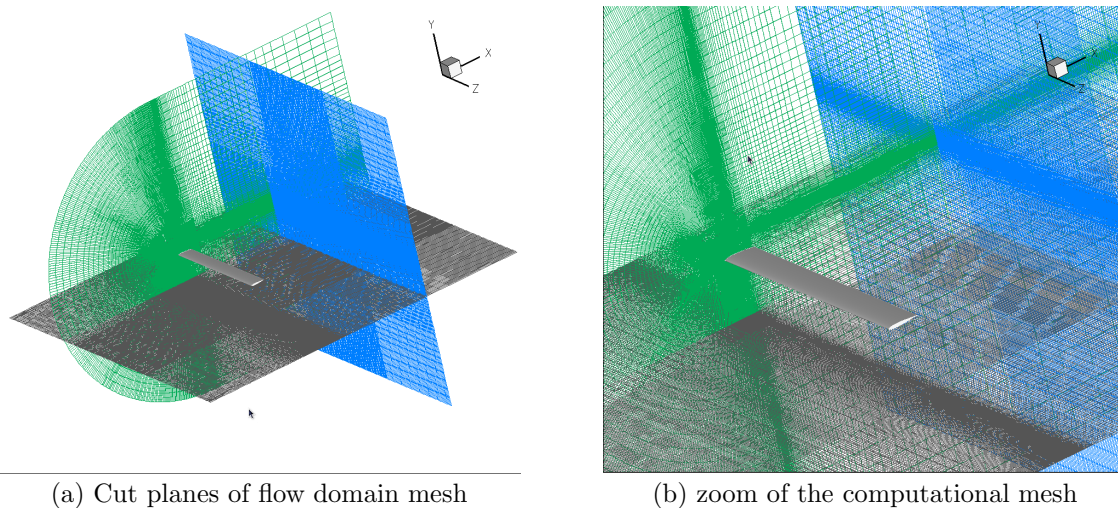


Figure 14. Computational mesh showing all degrees of freedom for the 5th order SD method

The flow Reynolds number is 2,000. Mach number is 0.1. The flow solution is first run to a steady state. The Mach number and pressure contours of the steady state solution are plotted in figure 15 (a) and (b). The steady state drag coefficient based on the wing reference area $S=4$ is $C_D=0.083$.

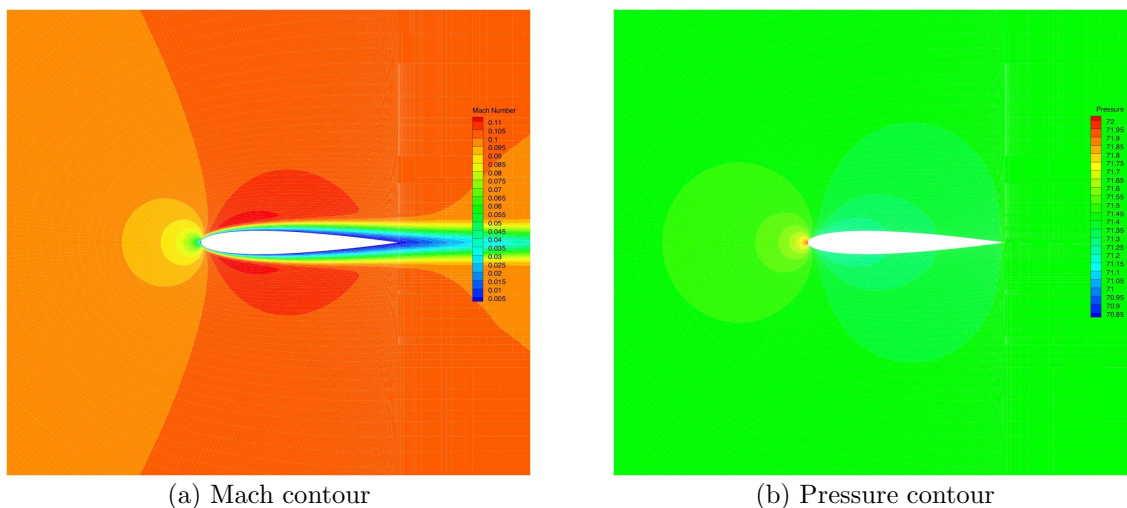
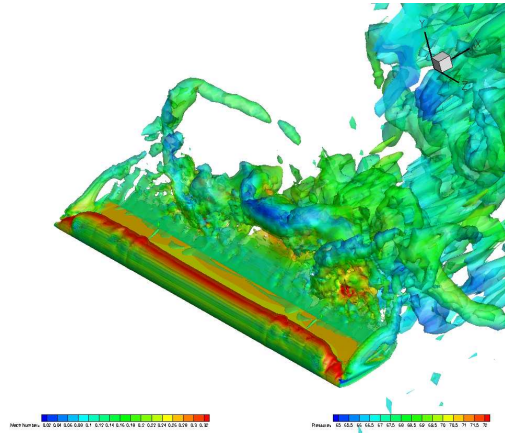


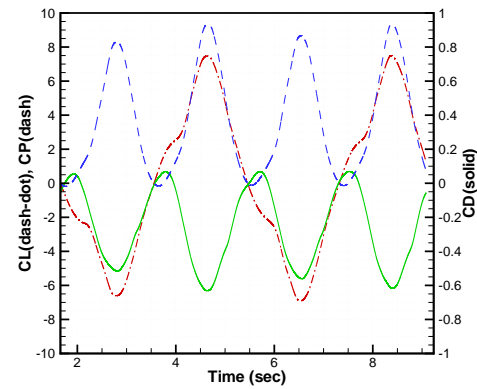
Figure 15. Steady flow over a naca0012 wing at $Re=2,000$ and $M=0.1$.

Starting with the steady state solution, simulations for three flapping wing motions have been computed until steady periodic solutions are obtained. The results are summarized in figure 16, 17, and 18. In figure 16 the flow fields of the three flapping wing motions are illustrated by plotting the flow entropy contours near the flapping wings at an instance when $t=8.6s$ (about $\frac{2}{3}$ through a downstroke). The contours are colored by the magnitude of Mach number. Wing surface pressure contours are also plotted (these are plotted again in figure 18 for clearer illustration). The lift, drag and power coefficients time histories for two complete flapping

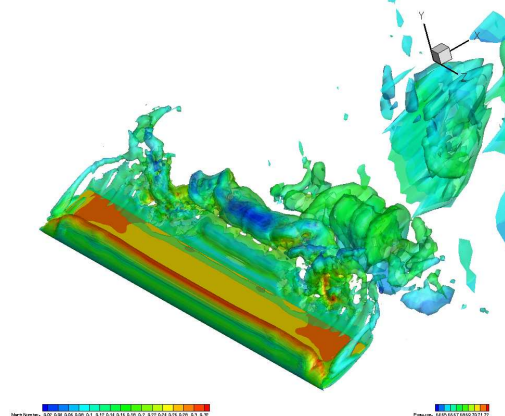
cycles are also presented in the right column of the same figure. From figure 16(b), (d), and (e), we find



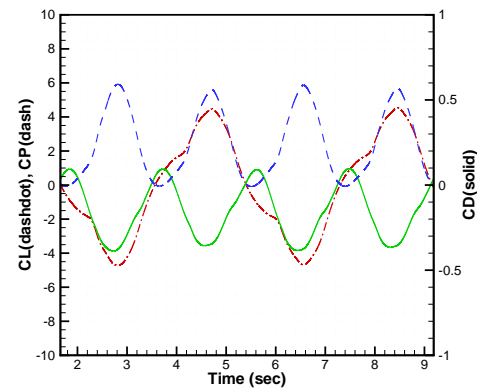
(a) Entropy contour of plunging motion



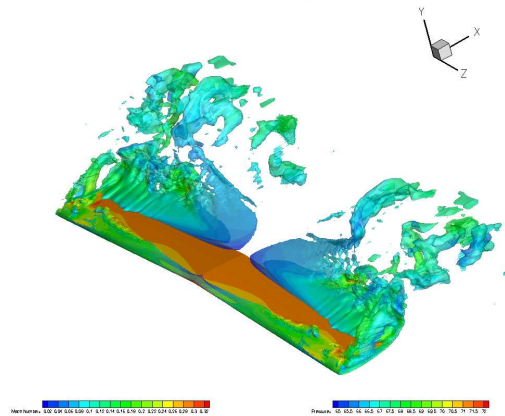
(b) C_L , C_D and C_p time histories of plunging motion



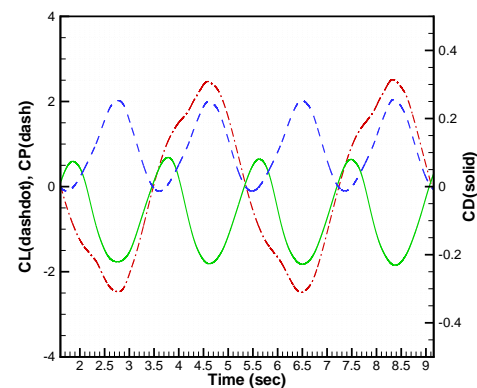
(c) Entropy contour of plunging-pitching motion



(d) C_L , C_D and C_p time histories of plunging-pitching motion



(e) Entropy contour of pitching motion



(f) C_L , C_D and C_p time histories of pitching motion

Figure 16. Simulation results of flow over a flapping naca0012 wing at $Re=2,000$ and $M=0.1$. (a), (c) and (e) show the flow entropy contours with Mach number colormap at $t=8.6s$. Wing surface pressure contours are also plotted. (b), (d) and (f) plot the lift, drag and power coefficients time histories for two complete flapping cycles.

that all three flapping wing motions produce net thrust. Pure plunging motion of the entire wing produces the most thrust of the three cases considered, but also at the expense of the largest power consumption. Adding a phase-lead pitching motion along the 1/3 chord reduces the net thrust coefficient but also reduces the power coefficient. The resulting aerodynamic efficiencies, measured by the ratio of time-averaged thrust coefficient and time-average power coefficient, are comparable for these two cases. By switching to pure

pitching wing motion, the aerodynamic efficiency however is much improved. Thrust is produced at about one quarter reduced power input than the previous cases. The different amount of energy being put into

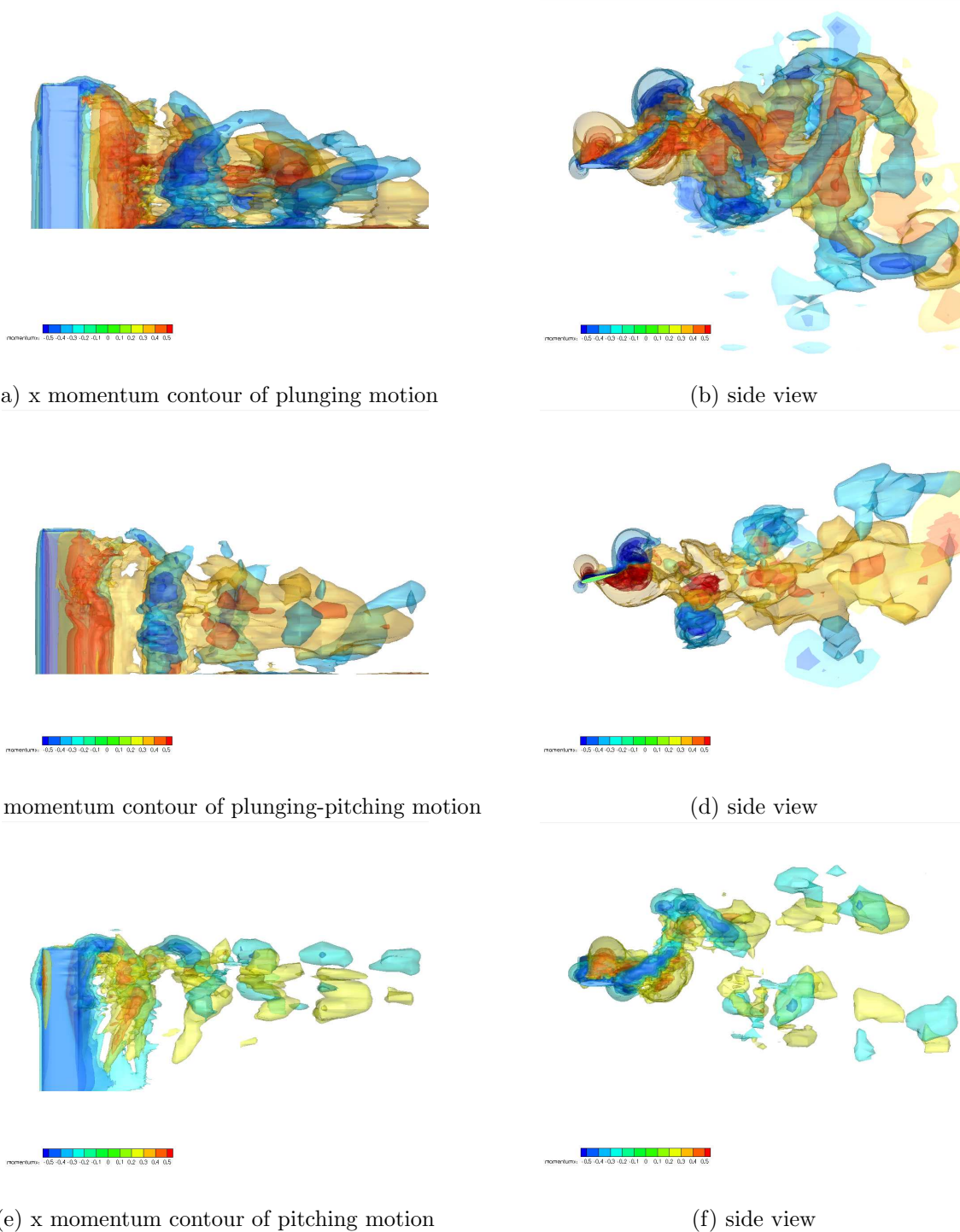


Figure 17. Simulation results of flow over flapping naca0012 wings at $Re=2,000$ and $M=0.1$. The freestream momentum contours are shown in the left column in top view, and in the right column in side view.

the flow field by the various flapping motions can be readily visualized by comparing the entropy contours and velocity magnitudes in the left column of the figure. The amount of thrust being produced by the three different flapping motions are visualized by plotting the net freestream momentum contours in figure 17. The presence of a momentum jet in the wake of the flow behind the wing is clearly visible for the plunging and the plunging-pitching motions. We observe that in both cases the flow pattern takes the form of a

coherent backward moving momentum jets being surrounded by a spiral stream of reversing flow. For the pitching wing motion, this type of flow pattern is confined to the wing tip region, and at a much reduced scale. Nevertheless, similar flow patterns are present in all three cases.

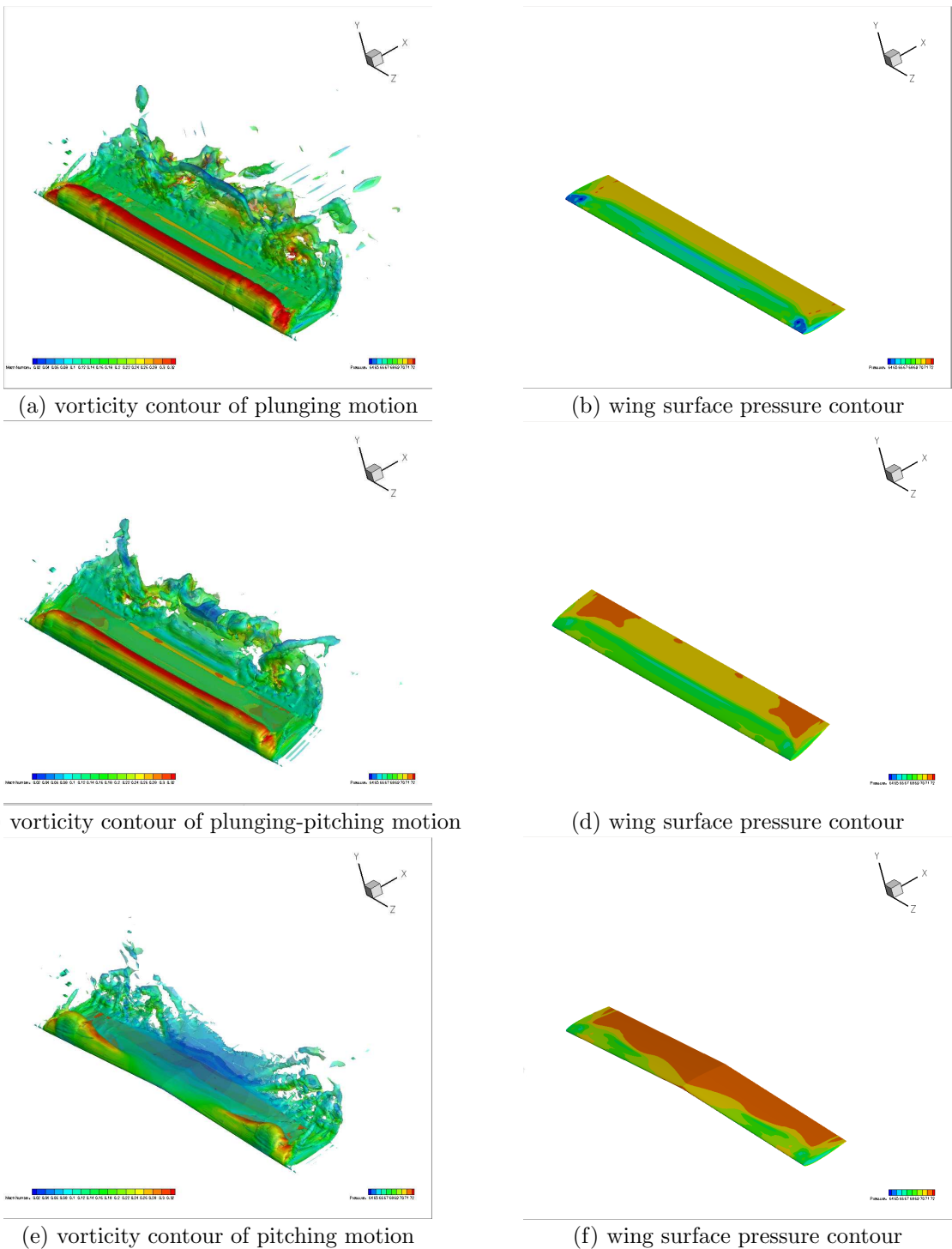


Figure 18. Simulation results of flow over flapping naca0012 wings at $Re=2,000$ and $M=0.1$. The vorticity contours with Mach number colormaps are shown in the left column. Wing surface pressure contours are plotted in the right column.

Finally, figure 18 (a), (c) and (e) plot the vorticity contours over the three flapping wings. These contours are again colormapped by the magnitudes of Mach number. Wing surface pressure contours are shown in figure 18 (b), (d) and (f). We observe that the distributions and magnitudes of low pressure regions on the

wing surfaces are closely related to the locations and intensities of the leading edge vortices.

IX. Conclusion

The objectives of the present study are two-folded. The first objective is related to numerical algorithm development. In this regard, we developed and validated a high fidelity unsteady three-dimensional flow solver based on spectral difference method. Three-dimensional simulations of flow over both a stationary and a plunging SD7003 airfoil produced results that compare well with existing experimental and computational studies. In addition, the favorable results coming out of the SD7003 airfoil test cases at transitional Reynolds numbers not only help to provide validation for our numerical methods, but also hint the future potential of using high order method as an efficient tool to resolve some fine scaled flow features without resorting to explicit LES models. While further testings in this regard are needed, this nevertheless illustrates another very encouraging aspect of the high order methods. The second objective is related to using the high fidelity numerical analysis tool to better understand flapping wing aerodynamics. Flow solutions of three flapping wing motions have been obtained. The chosen wing planform and flapping frequencies and amplitudes lead to thrust producing flapping flights in all three cases. We observe that large thrust can be obtained by maximizing the energy transfer from the flapping motion into as much surrounding air as possible. This is the case for the rigidly plunging wing, but this is not necessarily the most aerodynamically efficient. With the same Strouhal number based on the wing tip amplitude, pitching along the center line proved to be a more aerodynamic efficient way to produce thrust. While exploring the vast design space using the present high fidelity flow solver in search of the optimal flapping flyer can be very costly, the present study shows that current numerical algorithm developments allow considerable insight into the three-dimensional flapping wing flow features to be extracted and be made good use of in the design process.

Acknowledgement

This research work is made possible by the generous fundings from the National Science Foundation and the Air Force Office of Scientific Research under the grants 0708071 and 0915006 monitored by Dr. Leland Jameson, and grant FA9550-07-1-095 by Dr. Fariba Fahroo. The authors would like to acknowledge the support from the Stanford Graduate Fellowships program, the National Sciences and Engineering Research Council of Canada and the Fonds de Recherche sur la Nature et les Technologies du Québec.

References

- ¹D.J.Willis, E.R.Israeli, P.O.Persson, M.Drela, J.Peraire, S.M.Swartz and K.S.Breuer, *A computational framework for fluid structure interaction in biologically inspired flapping flight*, AIAA Conference, AIAA-2007-3803, Miami, FL, June 2007.
- ²D.J.Willis, J.Peraire, M.Drela, and J.K.White, *A numerical exploration of parameter dependence in power optimal flapping flight*, AIAA Conference, AIAA 2006-2994, San Francisco CA, June 2006.
- ³Y. Liu, M. Vinokur, and Z. J. Wang, *High-Order Multidomain Spectral Difference Method for the Navier-Stokes Equations on Unstructured Hexahedral Grids*, Communications in Computational Physics **Vol 2**, Number 2, pp 310-333 (2006).
- ⁴H. T. Huynh, *A flux reconstruction approach to high-order schemes including discontinuous Galerkin methods*, Number AIAA-2007-4079, AIAA Computational Fluid Dynamics Conference, 2007.
- ⁵A. Jameson, *A proof of the stability of the spectral difference method for all orders of accuracy*, J. Sci. Comput. (2010).
- ⁶V. V. Rusanov, *Calculation of interaction of non-steady shock waves with obstacles*, Journal of Computational Math Physics USSR, Vol. 1, pp.261-279, 1961.
- ⁷P. L. Roe, *Approximate Riemann solvers, parameter vectors, and difference schemes*, J. Comput. Phys. **43**, 357 (1981).
- ⁸P.O.Persson, D.J.Willis and J.Peraire, *The Numerical Simulation of Flapping Wings at Low Reynolds Numbers*, 48th AIAA Aerospace Sciences Meeting Including the New Horizons Forum and Aerospace Exposition, Orlando, Jan. 4-7, 2010.
- ⁹P. Castonguay, C.H. Liang, and A. Jameson, *Simulation of Transitional Flow over Airfoils Using the Spectral Difference Method*, AIAA-2010-4626, 40th Fluid Dynamics Conference and Exhibit, Chicago, Illinois, June 28-1, 2010
- ¹⁰R. Radespiel, J. Windte and U. Scholz, *Comparison of Laminar Separation bubble Measurements on a Low-Reynolds Number Airfoil in Three Facilities*, AIAA Paper 2005-5149, June 2005
- ¹¹R. Radespiel, J. Windte and U. Scholz, *Numerical and Experimental Flow Analysis of Moving Airfoils with Laminar Separation Bubbles*, AIAA Paper 2006-501, January 2007
- ¹²A. Uranga, P. Persson, M. Drela and J. Peraire *Implicit Large Eddy Simulation of Transitional Flows Over Airfoils and Wings*, 16th AIAA Computational Fluid Dynamics Conference, AIAA Paper 2009-4131 (2009)
- ¹³M.C. Galbraith and M.R. Visbal *Implicit Large Eddy Simulation of Low Reynolds Number Flow Past the SD7003 Airfoil*, 46th Aerospace Science Meeting and Exhibit, AIAA Paper 2008-225, (2009)

